

Full Length Article

Novel in-situ residual strain measurements in additive manufacturing specimens by using the Optical Backscatter Reflectometry



Shaoquan Wang*, Kaspar Lasn, Christer Westum Elverum, Di Wan, Andreas Echtermeyer

Department of Mechanical and Industrial Engineering, Norwegian University of Science and Technology (NTNU), Richard Birkelands vei 2B, 7491, Trondheim, Norway

ARTICLE INFO

Keywords:

Material extrusion
Residual strain
Manufacturing defect
Optical fiber
Optical Backscatter Reflectometry

ABSTRACT

Material extrusion (MEX) is a well established production method in additive manufacturing. However, internal residual strains are accumulated during the layer-by-layer fabrication process. They bring about shape distortions and a degradation of mechanical properties. In this paper, an in-situ distributed measurement of residual strains in MEX fabricated thermoplastic specimens is achieved for the first time. This innovative measuring system consists of an Optical Backscatter Reflectometry (OBR) interrogation unit connected to a distributed fiber optic strain sensor which is embedded during the MEX process. The characteristic residual strain distribution inside 3D printed components is revealed and numerically validated. The main mechanisms of residual strain creation and the sensing principles of in-situ OBR are described. A minimum measuring range of 4 mm and a spatial resolution of 0.15 mm were experimentally demonstrated. The potential of in-situ OBR technology for detecting invisible manufacturing defects was shown by a trial experiment.

1. Introduction

Material extrusion (MEX) is the most conventional additive manufacturing technology for plastics, also known as 3D printing. It offers great benefits to rapid prototyping and manufacturing applications [1]. MEX technology shows good potential in the automotive, aerospace, design and biomedical industries, due to its low cost, simplicity and environmental friendliness. Currently, it has already captured half of the 3D printing market [2]. The printer builds one layer at a time, with each subsequent layer being built directly on the previous. A wide variety of thermoplastic materials are available. However, a common negative characteristic is always recognized: accumulation of residual stress and strain during the material build up [3]. More specifically, the feedstock thermoplastic experiences a melting and rapid cooling cycle and a consequent phase transformation from molten to solid state during the deposition of each layer. Residual stress mainly arises from the shrinkage of the thermoplastic during the phase transformation and accumulates during the layer-by-layer build up process in MEX [4]. Residual stresses can significantly affect the dimensional accuracy, cause warping, interlayer delamination, cracking, decrease of mechanical properties and even interrupt the printing procedure when the specimen detaches from the printing bed. This kind of disadvantage, innate to layer-by-layer build-up hinders the application of the MEX.

An experimental research study was carried out by Dao et al. [5] to

evaluate the dimensional accuracy of models made by MEX. The results show that the dimensional inaccuracy of the MEX production is mainly induced by the material shrinkage after experiencing a phase transformation from a semiliquid to a solid state during the melting and cooling cycles. As reported by Casavola et al. [6], accumulation of residual stress due to the rapid heating and cooling cycles of thermoplastic can seriously affect the shape and the final dimensions of the parts. A FEA model was developed by Zhang and Chou [7] to simulate the shape distortion from the MEX process. The results show that part distortions are related to the stress accumulation during the deposition. Es-Said et al. [8] concluded that volumetric shrinkage, induced by phase transformation during solidification, caused weak interlayer bonding and high porosity resulting in reduced mechanical properties. Wang et al. [9] showed that decreasing the glass-transition temperature and linear shrinkage rate of the feedstock material is helpful for the reduction of inner stresses responsible for warp deformation. These results indicate that the contraction of thermoplastics during MEX processing is believed to be the main cause of distortions, interlayer delamination and degradation of mechanical properties. Hence, for eliminating these negative effects, processing optimization aiming at reducing residual strains can improve the strength and the shaping precision. It is regarded as an important issue for successful industrial application of the MEX technology.

Evaluating residual strain distribution is essential for MEX

* Corresponding author.

E-mail address: shaoquan.wang@ntnu.no (S. Wang).

<https://doi.org/10.1016/j.addma.2020.101040>

Received 11 September 2019; Received in revised form 17 December 2019; Accepted 2 January 2020

Available online 03 January 2020

2214-8604/ © 2020 The Authors. Published by Elsevier B.V. This is an open access article under the CC BY license (<http://creativecommons.org/licenses/by/4.0/>).

parameter optimization [10]. Unfortunately, it is quite challenging to measure residual strains during MEX by using traditional measurement technologies. To the best of the authors' knowledge, only one series of promising works in this field was reported by Kantaros et al. and Kouziatza et al. over the recent years [10,11]. In this research, an in-situ point strain measurement was performed through one Fiber Bragg Grating (FBG). A short FBG was embedded at the midplane of the samples. The residual strain at the centroid of the specimen, where the grating was located, was viewed as the average residual strain of the whole specimen. However, point sensors present serious limitations in application. For instance, the measured strain value from FBG can be distorted, when the grating of the FBG fiber passes through a manufacturing defect, like an under/over-filled region or distorted part of the structure. Additionally, the number of point sensors necessary to obtain a global strain monitoring, becomes impractically high for large specimens. The lack of reliable in-situ and distributed measurement approaches for residual strains impedes the development of the MEX technology.

In this study, a novel approach for measuring the solidification-induced residual strain distribution in MEX fabricated specimens was achieved for the first time. The measuring system consists of an Optical Backscatter Reflectometry (OBR) interrogation unit connected to a standard single mode optical fiber embedded in the component during the MEX process. Based on Rayleigh backscattering, distributed strain sensing is achieved along the axis of the optical fiber. A non-invasive embedding procedure is presented and validated from micro to macro scale. A comparison between the in-situ OBR and the electrical strain gauge validates the reliability of the new approach. A characteristic horizontal residual strain distribution and the vertical average residual strain distribution were revealed inside MEX fabricated specimens. A simplified description is presented that captures key mechanisms of residual strain creation in MEX. The molecular behavior of the feed-stock material induced by temperature evolution during the MEX process was characterized by a differential scanning calorimetry (DSC) instrument and by an infrared camera. The effects of the OBR post-processing parameters and specimen dimensions on the measurement results were analyzed. Moreover, the possibility of detecting manufacturing defects by this innovative method was also demonstrated.

2. Materials and methods

2.1. OBR instrument and the optical fiber strain sensor

As shown in Fig. 1 (a), the distributed optical fiber strain sensor (DOFS) is SMB-E1550H fiber from OFS Fitel, LLC. It is a silica/silica/polyimide fiber with a core diameter of 6.5 μm , a clad diameter of 125 μm and a coating diameter of 155 μm . It is a single mode fiber (SMF) with an operating wavelength of 1550 nm. The polyimide coating enables working temperatures between -65 $^{\circ}\text{C}$ and +300 $^{\circ}\text{C}$. The SMF is spliced to a secondary coated optical fiber (SCOF), whose end is a connector port for transmitting the sensing signal to the interrogator. An "OBR 4600" reflectometer from Luna Instruments (Luna Innovations Incorporated, Virginia, USA) is used as the interrogator device as shown in Fig.1 (b).

2.2. Specimen preparation

The MEX printed test specimens were built on a PRUSA I3 MK2S 3D printer (Fig.1 (c)). A 1.75 mm PLA filament (3DNet) was selected for this research. PLA is the most common and representative thermoplastics for MEX printing, very popular in application and also preferred as an environmentally-friendly material. In principle, similar experiments could be carried out with any common 3D printing materials. The alignment holders (Fig.2 (a)) were printed from 1.75 mm ABS filament (3DNet), because it enables sufficient thermal stability on the heating bed during printing. Cura software is used to control the

printing process. The printing parameters are summarized in Table 1. All specimens were infilled by PLA roads at 90 $^{\circ}$ with respect to the X direction of the specimen, as shown in Fig. 1 (d). The X-Y-Z coordinates defined in Fig. 1 (d) will also be used in the following sections.

In order to investigate the effects of specimen geometry on the in-situ OBR measurement results, eight sets of samples were printed as shown in Table 2. The length of X axis of the specimens of group 1 (G11 ~ G15) increases from 15 mm to 80 mm, while both the width (Y axis) and height (Z axis) remain at 15 mm and 20 mm respectively. The specimens of Group 2 (G21 ~ G23) have different widths as the unique variable parameter.

2.3. Sensor embedment

In order to achieve in-situ measurements of residual strains, the SMF part of the sensor needs to be embedded into the MEX fabricated specimen. A schematic illustration of the SMF embedding procedure as well as the final printed specimen after embedding are shown in Fig. 2. Prior to the experiment, the G-code was rewritten to pause the 3D printer at a self-defined deposition layer, and resumed the printing process after a self-defined time period. A methodology for SMF integration during the building procedure is briefly described below:

(1) Alignment holder assembly

An alignment holder was designed to assist the placement of the SMF during printing. The alignment holder contains plug-in component blocks with different thickness (Fig.2). Each component has a groove covered by a soft double-face tape to fix the SMF. By assembling blocks, two holders are able to support the optical fiber and assure the sensors' positioning at a specific height.

(2) SMF embedding

When the layer where the optical fibre should be implemented was reached, the 3D printer was paused automatically for 15 s. The SMF was then hand placed on the surface of the last deposited layer along the X axis and fixed by tapes on the holders as shown in Fig.2. Subsequently, the printing process was resumed. A new layer was built on the previous, and the SMF became encapsulated by extruded thermoplastic.

(3) Replacement and cooling

Each printed specimen was detached from the build platform right after finishing the print. Measurements were taken after the specimen had gradually cooled down to room temperature.

2.4. Optical Backscatter Reflectometry

2.4.1. OBR working principles

Optical Backscatter Reflectometry (OBR) is an optical frequency-domain method that measures Rayleigh backscatter over the length of the optical fiber. Rayleigh scattering happens when a photon penetrates a medium composed of particles whose sizes are much smaller than the incident photon wavelength. In this scattering process, the energy of the incident photon is conserved but its direction is changed randomly. In an optical fibre, silica molecules moved randomly in the molten state and froze in place during fabrication, leading to random fluctuations of the refractive index, on a scale smaller than the optical wavelength. In the OBR system, a laser source sends the incident light through the optical fiber. Rayleigh backscattering happens along the entire fiber length and its pattern acts as a unique fingerprint for each fiber. The Rayleigh backscattering in an optical fiber has similarities with fiber Bragg gratings (FBG): changes in physical length induce a frequency shift of the reflected spectrum [12–14]. These Rayleigh backscattering spectral shifts (RBS) are measured and scaled to give distributed

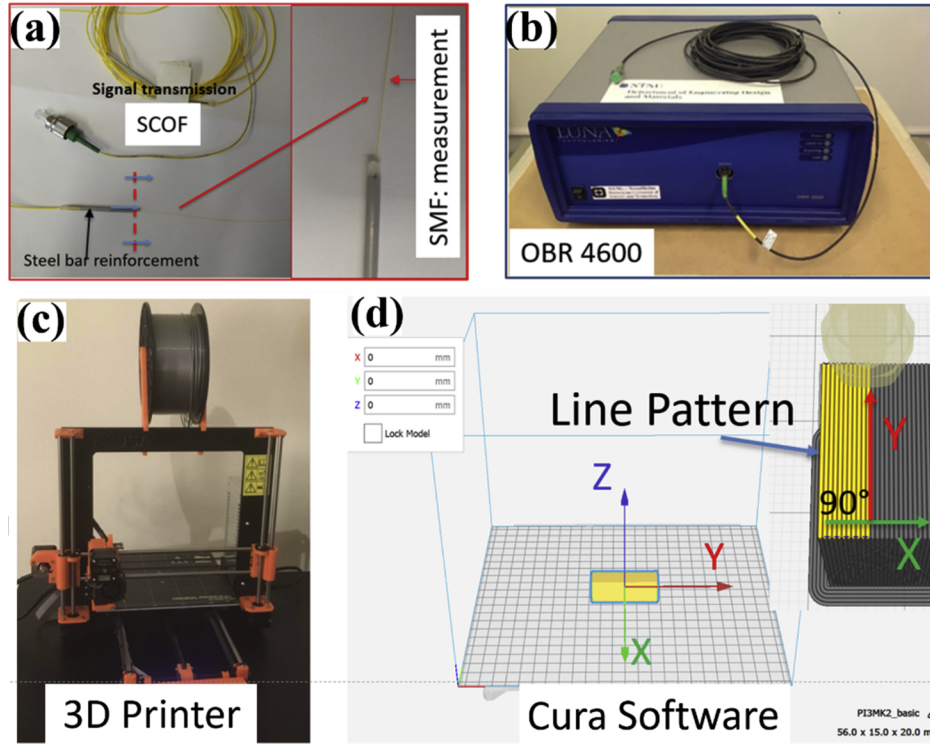


Fig. 1. Measurement and manufacturing devices: (a) Distributed optical fiber strain sensor, (b) LUNA OBR 4600 interrogator apparatus, (c) Prusa 3D printer, (d) Infill control software.

temperature or strain measurements with a high sensitivity and spatial resolution. The OBR has been applied successfully in distributed optical fiber sensor (DOFS) systems for monitoring of strain and temperature in different materials [15–20]. Heinze et al. [15] reported a new experimental method based on OBR to measure strains due to cure shrinkage in large volumes of hardening epoxy. In the study of Billon et al. [16], OBR was used as a truly distributed sensing system to monitor the strain of a concrete structural element tested in four-point bending. OBR was also adopted by Villalba et al. in detecting and monitoring the presence of damage-induced cracks in concrete structures [17]. Under ideal conditions, the DOFS based on OBR have a spatial resolution of under 1 mm and the strain resolution can be as good as 0.001 % [15,18,19]. This enables approximately thousand sensing points for every meter length of the optical fiber. Thus, the OBR system can be used to map strain distributions of a structure rather than a rough extrapolation from a few point measurements [20].

2.4.2. OBR signal demodulation

The RBS ($\Delta\nu$) between the spectra of free and loaded SMF are demodulated using the OBR Desktop v3.13.0 software. Identical to the response of an FBG, the $\Delta\nu$ of the spectrum induced by environmental perturbation can be given as [18]:

$$-\frac{\Delta\nu}{\nu} = K_T \Delta T + K_\epsilon \epsilon \quad (1)$$

Where ν is the mean optical frequency, and K_T and K_ϵ are the temperature and strain coefficients, respectively.

$$K_T = \alpha + \xi \quad (2)$$

$$K_\epsilon = 1 - \frac{n_{\text{eff}}^2}{2} (p_{12} - \mu(p_{11} + p_{12})) \quad (3)$$

K_T is a sum of the thermal expansion coefficient $\alpha = (1/\Lambda)(\partial\Lambda/\partial T)$, Λ is the volume of the optical fiber, and the thermo-optic coefficient $\xi = (1/$

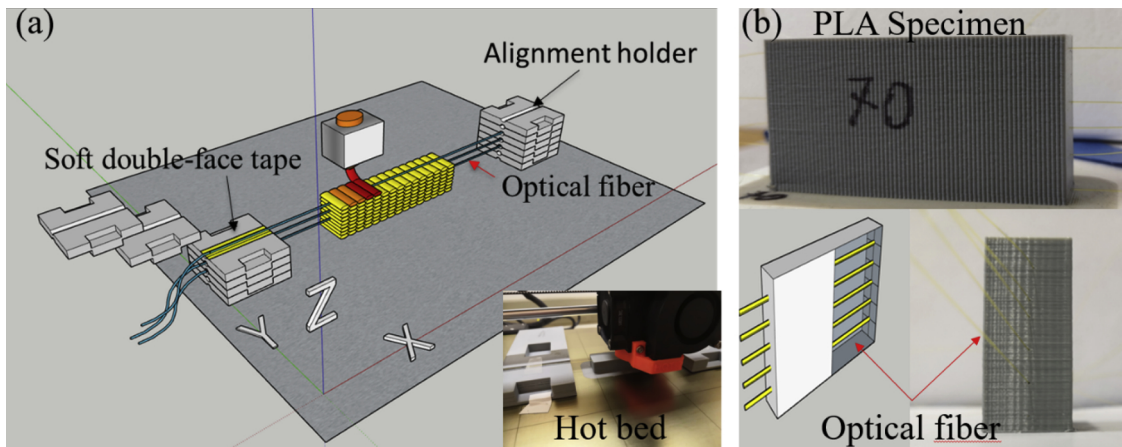


Fig. 2. A schematic illustration of the SMF embedding procedure (a) and a MEX fabricated specimen with the SMF ingressing and egressing at several locations (b).

Table 1
Printing parameters.

Layer height	Print speed	Print temperature	Build Plate temperature	Infill pattern	Infill direction	Build plate adhesion	Fan cooling
0.2 mm	30 mm/min	205 °C	60 °C	Lines	90°	Brim	Open

Table 2
MEX Specimen dimensions.

Specimen No.	Length (mm)	Width (mm)	Height (mm)	Infill density
G11	15	15	20	100 %
G12	25	15	20	100 %
G13	40	15	20	100 %
G14	56	15	20	100 %
G15	80	15	20	100 %
G21	56	15	20	100 %
G22	56	25	20	100 %
G23	56	50	20	100 %

$n(\partial n/\partial T)$, with typical values of $0.55 \times 10^{-6} \text{ }^\circ\text{C}^{-1}$ and $6.1 \times 10^{-6} \text{ }^\circ\text{C}^{-1}$ for Germanium-doped silica core fibers. K_e is a function of the group index n ; the components of the strain-optic tensor, p_{ij} ; and Poisson's ratio μ . Typical values for germanium-doped silica are reported in [18]: $K_e = 0.78$, and $K_T = 6.45 \times 10^{-6} \text{ }^\circ\text{C}^{-1}$.

2.4.3. Residual strain sensing by in-situ OBR technology

Since the SMF is embedded into a substrate material, the generalized demodulation equation is modified to account for residual strains in MEX. Before embedding, the optical fiber (without any mechanical loading, at room temperature) is connected to the OBR interrogator and the reference spectrum is recorded. In the next step, the SMF is embedded into the specimen during MEX. After printing, the specimen is removed from the hot bed and cooled down to room temperature, and a measurement spectrum was recorded from the specimen after cooling. In general, thermally induced strains are applied to the SMF as a result of the mismatch in the coefficients of thermal expansion (CTE) between the SMF (α_f) and the matrix material (α_m). Eq.(1) is modified as [10]:

$$-\Delta\nu/\nu = K_e(\epsilon_{res} + (\alpha_m - \alpha_f)\Delta T) + K_T\Delta T \quad (4)$$

ϵ_{res} accounts for the solidification-induced residual strains during MEX and ΔT is the temperature difference between the initial reference and the final measurement. In this research, the temperature of the reference and measurement test is the same T_{room} i.e. $\Delta T = 0$ and Eq. (4) reduces to:

$$-\Delta\nu/\nu = K_e\epsilon_{res} \quad (5)$$

Eq.(5) can be further converted to:

$$\epsilon_{res} = -\frac{\bar{\lambda}}{CK_e}\Delta\nu \quad (6)$$

where $\bar{\lambda}$ is the center wavelength of the scan and C is the speed of light inside the fiber. The scan center wavelength is 1550 nm. The constant K_e of 0.780 can be substituted to yield the following conversion factor:

$$\epsilon_{res} = -6.67(\mu\text{E}/\text{GHz}) * \Delta\nu. \quad (7)$$

By using this conversion factor, the solidification induced residual strain ϵ_{res} in MEX along the axis of embedded SMF can be calculated from RBS ($\Delta\nu$).

2.5. Temperature profile measurement and the DSC

The temperature evolution during the MEX was measured using a FLIR A655sc IR camera at 50 frames per second at full frame 640×480 resolution. The approximate distance from the lens to the target was

500 mm.

In order to fully understand the mechanisms of residual strain creation and ensure the strain transfer effectiveness of the SMF/PLA interface, the thermal transition and corresponding molecular behavior of PLA and SMF coating material during the MEX process were investigated by DSC. More details will be discussed in subsection 3.1 and 3.3. DSC samples were prepared from chopped feedstock PLA filament before printing and G14 specimen separately. Chopped SMF was used as the optical fiber coating DSC sample. Measurements were performed on a DSC-250 instrument (TA instruments, New Castle, DE) from $0 \text{ }^\circ\text{C}$ up to $300 \text{ }^\circ\text{C}$, at a heating rate of $10 \text{ }^\circ\text{C}/\text{min}$, and kept at isothermal state for 10 min, then cooled down to $0 \text{ }^\circ\text{C}$ at a cooling rate of $10 \text{ }^\circ\text{C}/\text{min}$. Nitrogen atmosphere was employed during the experiment, using a 50 ml/min flow rate.

2.6. Micro-characterization

All sample cross-sections were prepared from a G14 specimen by polishing in Meta 250 autopolisher (Buehler Inc, USA) using low speed and water cooling. A RH-2000 digital microscope (Hirox. Ltd, France) and a FEG Quanta 650 Environmental scanning electron microscope ESEM (Thermo Fisher Scientific Inc., USA) were used to observe possible manufacturing flaws induced by SMF embedding.

3. Results and discussion

The in-situ OBR has never before been adopted for MEX fabricated thermoplastic components according to the best of this author's knowledge. Prior to measuring residual strains, preliminary tests were conducted to validate the in-situ OBR measurement approach. Subsequently the MEX fabricated specimens will be measured in both horizontal and vertical directions. The effects of specimen dimensions on the measurement results are discussed. Combined with the results of DSC and infrared camera testing, the key mechanisms of residual strain creation in MEX are investigated and a simplified description for the residual strain creation is presented. Finally, the possibility of detecting manufacturing defects by this innovative method will be presented.

3.1. Validation of in-situ OBR technology applied in MEX

3.1.1. Practical challenges and countermeasures

The practical challenges related to the use of in-situ OBR technology in MEX are mainly twofold: the first one is that the SMF embedding procedure is expected to be non-invasive with little disturbance to the MEX process. Another concern is related to the strain transfer effectiveness between the sensor and the surrounding material.

The SMF is expected to be straight during embedding. Nevertheless, the moving nozzle may displace the SMF during deposition, leading to damage or bending of the optical fiber. A broken optical fiber can not transfer a sensing signal, and bending of the optical fiber can induce noise into the data. These hidden dangers were mitigated by selecting an appropriate layer thickness of 0.2 mm, slightly larger than the diameter of the SMF. Fig.3 shows the micrographs taken from three cross-section planes of the embedded SMF. As shown in cross-section 1 in Fig.3 (b), the SMF is entirely encapsulated by the PLA material through the surfaces in both the substrate and embedding layers without pinching. In cross-sections 2 and 3 in Fig.3 (c) and (d), the embedded SMF appears straight without bending or visible damage. In SEM

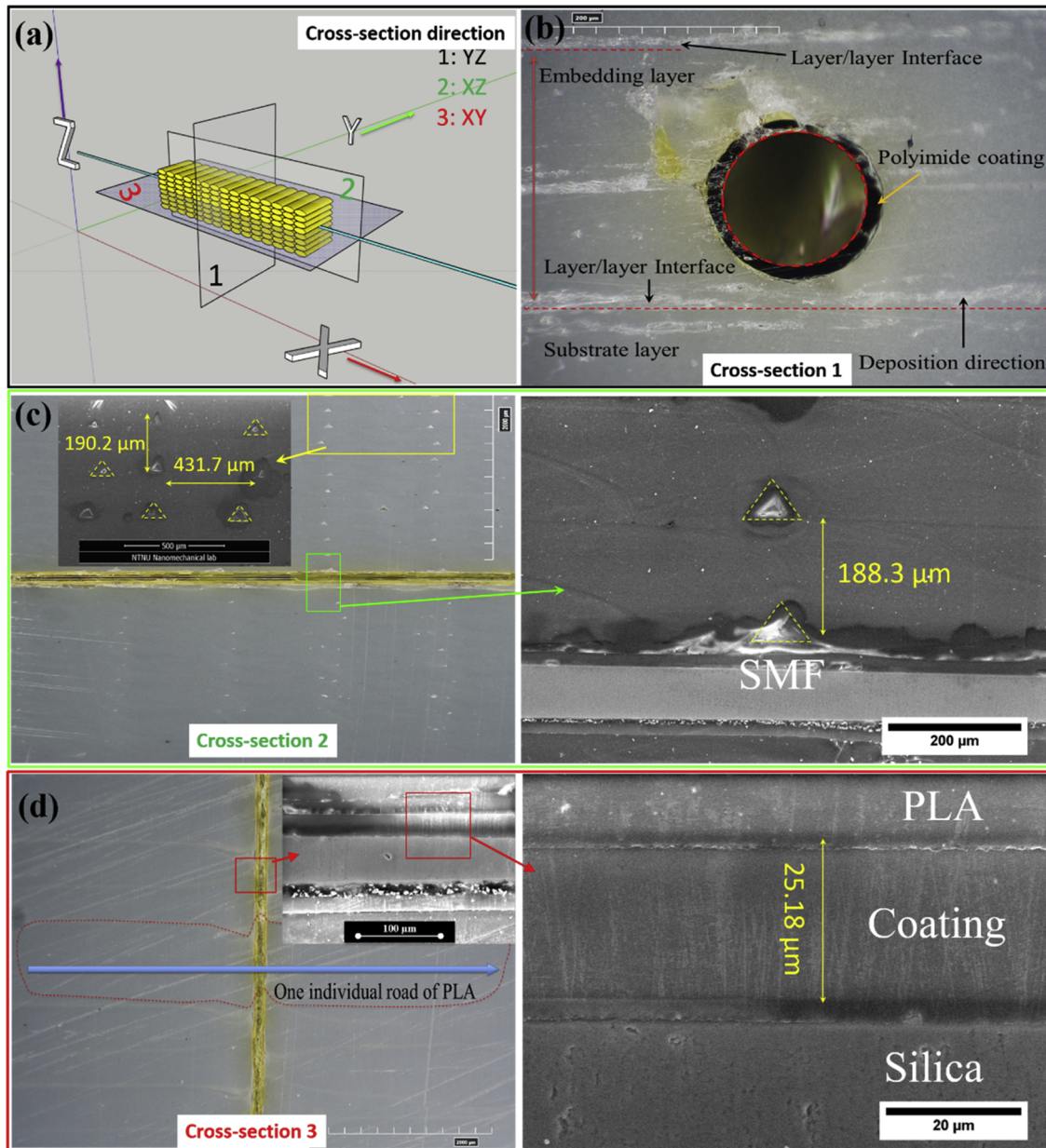


Fig. 3. Micrograph analysis of embedded SMF: (a) Illustration of sampling position in specimen, (b) Optical micrograph of cross-section 1, (c) Optical and electron micrograph in cross-section 2, (d) Optical and electron micrograph in cross-section 3.

images of Fig. 3 (c), there are no voids surrounding the optical fiber. The special patterns of near triangular voids are proved to be intrinsic to the MEX, as the vertical and horizontal distances between two adjacent voids are corresponding to the layer thickness and nozzle diameter separately [23]. The SMF/PLA interface and Coating/Silica interface of SMF are well bonded in SEM images of Fig. 3 (d). There are no delaminations or cracks generated by the SMF embedment. In conclusion, the embedment process brings no disturbance on the MEX process and no visible damage on the SMF itself.

When the SMF is used as a strain sensor, the strain of the surrounding material needs to be transferred into the optical fiber by the PLA/ SMF interface. As mentioned by Grave [18], when the coating material of the SMF becomes soft, the strain of its surroundings can not be transferred into the fiber by shear accurately. Thus, the interface compliance will affect the accuracy of the measurement. In the present work, the PLA/SMF interface is mainly composed of the polyimide coating on the SMF. In order to assure the strain transfer effectiveness, the polyimide coating needs to remain in the glassy state during the

MEX process. Thus, thermal transitions of polyimide are important physical characteristics for the application of the OBR technology. Specifically, the frozen molecular motions of thermoplastics are activated during glass transition, hence the brittle and glassy polymer becomes soft and flexible. In this case, the polyimide coated SMF is no longer suitable for strain measurements. Fig. 4 shows the DSC heating-cooling thermograms for the polyimide coating of the SMF. No endothermic or exothermic peaks emerged in the DSC curve up to 300 °C. The polyimide coating remains in the glassy state during printing, with sufficient stiffness to transfer residual strains from the MEX process to the silica of the optical fiber.

3.1.2. OBR based strain sensing compared to electrical strain gauges

As a distributed strain sensing system, the entire embedded SMF is required to be evenly bonded with the surrounding matrix to enable continuous strain field measurements. Thus, an initial proof of concept tensile test was carried out to investigate the SMF/PLA interfacial bonding. The strain values were measured by the OBR and electrical

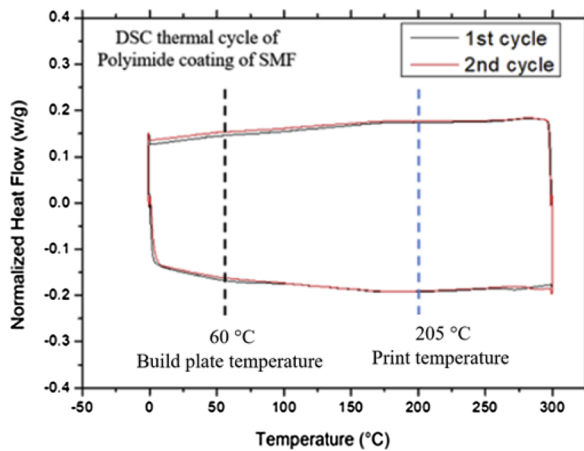


Fig. 4. DSC curve of the SMF polyimide coating.

strain gauges (SG) simultaneously to compare the strains from this OBR method with a traditional method. The SMF was embedded in a 3D printed dog-bone specimen (220 mm × 25 mm × 2 mm), while two SGs were bonded on the surface by cyanoacrylate. A hole ($\varnothing = 2$ mm) was built in the middle of the tensile specimen to investigate the measurement capability of the OBR technology near sharp strain gradients. The MEX-fabricated specimens were infilled in a line pattern perpendicular to the long axis of the specimen. The SMF was applied in the mid-plane of the specimen with a distance 1 mm from the hole and the SGs were bonded 0 mm and 25 mm from the hole, as shown in Fig. 5 (a). The tensile test was conducted in an Instron 5 kN test machine and the strain measurements were taken by in-situ OBR technology and SGs (FLAB-6-17, 6 mm × 2.2 mm, 120 Ω , Tokyo Measuring Instruments Laboratory Co., Ltd.) at the same time instance.

Fig.5 shows the strain measurements from the OBR and two electric strain gauges. A continuous strain field along the specimen length was successfully obtained through the OBR method. A gradual strain increase over the gauge length of the specimen was exhibited in the strain field. The highest values were obtained at the equator of the hole, which coincides with the expected strain concentration location. A general agreement can be seen between the results of SGs and the in-situ OBR technology, but there are small deviations. The SG1 and SG2 showed tensile strains of similar magnitude, but always less than the OBR results. The difference between OBR and SG values at higher stresses (225 N ~ 380 N) is 14 %, while it is smaller at lower stresses (0 N ~ 225 N). This phenomenon arises from the intrinsic characteristic of applying SGs. The SMF is more accurate, as it measures strains over a

very narrow width (155 μm). The SG measures an average over its width (2200 μm), where the lower strains dominate. The averaging effect over a spatially changing strain field is most likely the main cause for the strain discrepancy. Secondly, the mislocation between the SMF and SG is inevitable. The whole SG area is more offset from the hole edge (stress concentration region) compared to the SMF, naturally leading to lower peak strains than SMF. Additionally, the strain may not always be transmitted to the SG completely due to the possible partial debonding between SG and specimen surface during tension. In conclusion, the embedded SMF seems evenly and well connected with PLA and no PLA/SMF interfacial debonding happens before 10,000 μe . The embedded SMF can be viewed as a reliable distributed strain sensor in the MEX fabricated specimen. Especially, when a steep variation exists in the strain field, applying the in-situ OBR method can measure strains more accurately than by using single-point SGs.

3.2. Experimental measurement results

3.2.1. Residual strain distribution

The data from the SMF were measured by OBR interrogator and analyzed by the OBR Desktop v3.13.0 software. In post-processing, the software defines many virtual strain gauges along the length of the SMF. All virtual strain gauges have the same gauge length (GL) and sensor spacing (SS) between them as shown in Fig.6 (a). After comparing the reference and measurement spectrum, strain of each virtual sensor is calculated from an average RBS on the corresponding GL part. One SMF is embedded in the midplane of a specimen (56 mm × 15 mm × 20 mm) in the X direction during the MEX process. When GL and SS parameters are both set to 8 mm, the embedded SMF can be viewed as an array of 7 virtual strain gauge sensors placed back-to-back along the axis of SMF. Each measurement point corresponds to one virtual strain sensor, which shows the average strain of the GL = 8 mm long section of the SMF. As shown in Fig.6 (b), the MEX induced residual strain value on each virtual strain sensor is negative, which indicates shrinkage strain. In the horizontal direction, experimental measurement results show similar negative values inside the specimen, except for the two points from the egress parts of the embedded SMF. The strain differences in the egress parts may be induced by the signal outliers in the measurement, which will be briefly discussed in subsection 3.2.2. Contrary to traditional casting and injection moulding where the residual strains increase from the exterior to the interior and lead to a symmetric tapered distribution [15,21], the MEX shows a horizontally uniform distribution of residual strains as shown in Fig.6 (c).

In order to characterize the residual strain distribution in both

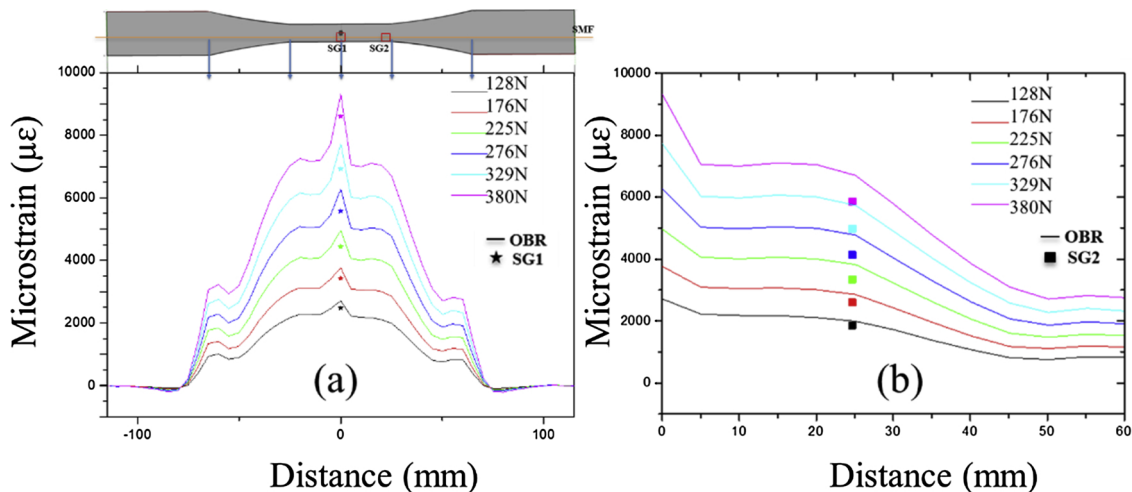


Fig. 5. Strain measurements from the OBR and electric strain gauges during a tensile test.

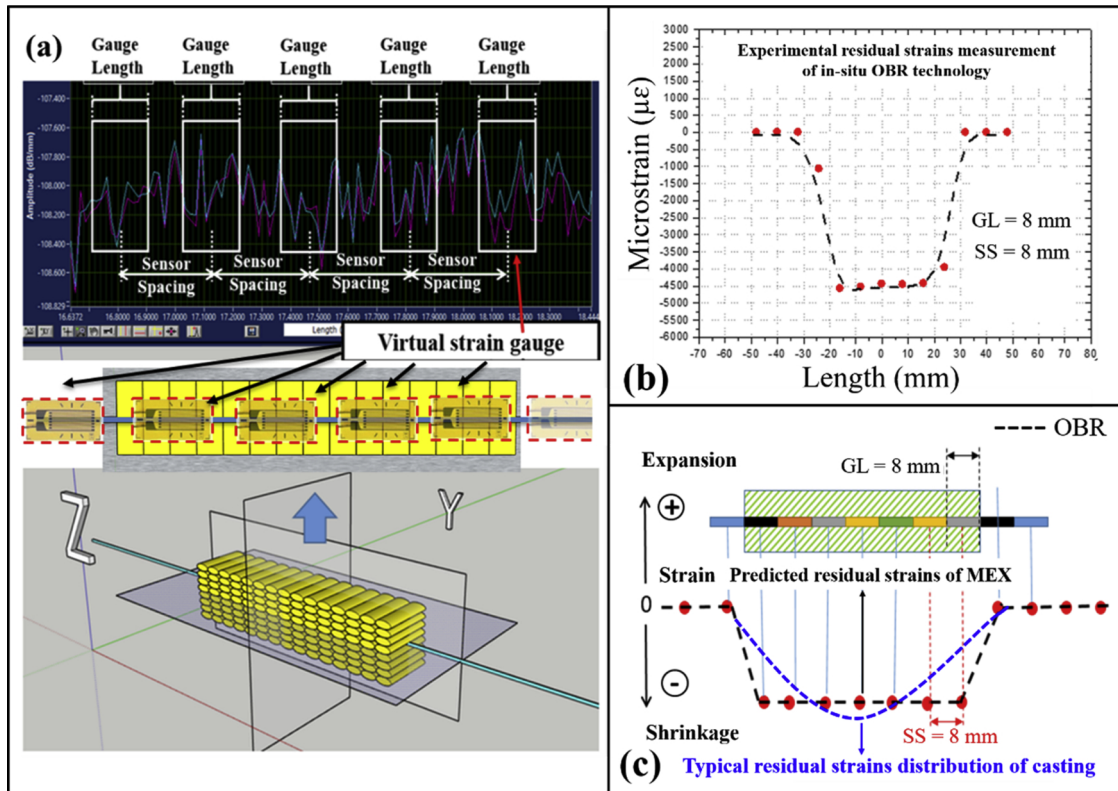


Fig. 6. Schematic illustration of post-processing parameters (a), experimental measurement of residual strains in MEX (b) and comparison between the residual strain distribution in casting and MEX (c).

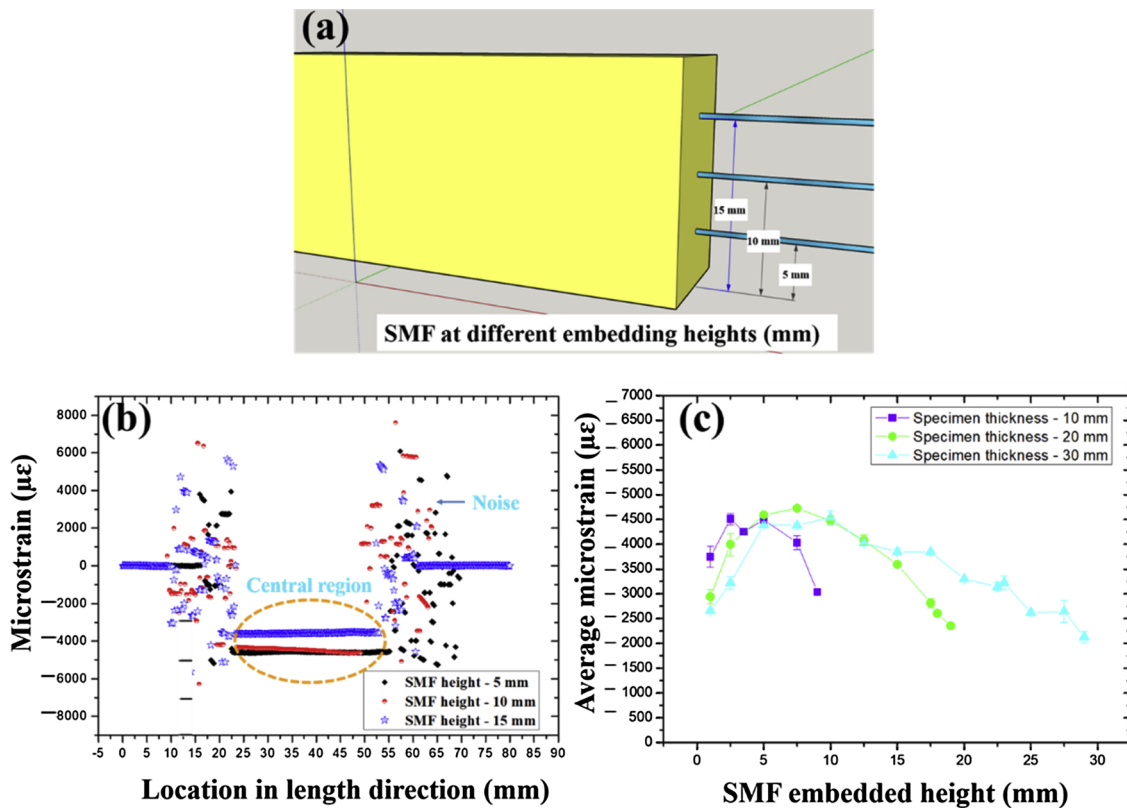


Fig. 7. Residual strain distribution in specimens: (a) Illustration of multiple SMF embedding, (b) Measurement of residual strain distribution in length direction at different heights in 20 mm thick G14 specimen, (c) Calculated average residual strain distributions in thickness direction of specimens with thickness of 10 mm, 20 mm and 30 mm.

length (horizontal) and thickness (vertical) directions, the SMFs were embedded in the midplane at different heights (in Z direction) along the length (in X direction) of the specimen (56 mm × 15 mm × 20 mm) as shown in Fig. 7 (a). The adopted OBR parameters here are 4 mm GL and 0.15 mm SS, enabling high resolution measurements. A short overview about the effects of post-processing parameters on the measured strains is given in Appendix A. As shown in Fig. 7 (b), no regular and continuous data can be observed in the ingress and egress parts of embedded SMF, however the data measured in the central region of embedded SMF are constant. The scattered outliers are viewed as noise while the constant values in the central region are believed to be representative of the residual strain in the MEX fabricated specimen. More details related to measurement noise will be discussed in chapter 3.2.2 and 3.4. In the length direction of G14 specimen, the residual strains in the bottom, middle and top layers all show a uniform distribution simultaneously. In this research, the mean value of the central region from the embedded SMF is used as the average residual strain of the layer where the SMF is in. As shown in Fig. 7 (c), the variation of average residual strain values shows a well-defined height dependency. The average residual strain increases from the bottom to about one third of specimen thickness and then starts to decrease until the top of the specimen. Such 'parabolic trend' of average residual strains in thickness direction of MEX fabricated PLA has never been reported before. Two additional specimens with a lower thickness (56 mm × 15 mm × 10 mm) and a higher thickness (56 mm × 15 mm × 30 mm) were measured to verify the repeatability of the parabolic trend in average residual strains. As shown in Fig. 7 (c), the specimens with different thicknesses all show similar parabolic distribution of average residual strains in the thickness direction. The most extreme residual strains develop inside the specimen, at ca. 1/3 height from the build plate.

3.2.2. Effect of specimen dimensions

The in-situ OBR technique may be applied to MEX-fabricated specimens of different dimensions. It is therefore of interest to investigate how the geometrical size of specimens affects the OBR measurement. One SMF was embedded within the midplane of the specimen built as shown in Table 2. As shown in Fig. 8 (a), the obtained data is scattered along the embedded SMF randomly, and no constant and continuous data can be observed in the short G11 specimen. For G12, the embedding length of the SMF increased to 25 mm and the outliers are still apparent in the ingress and egress parts of embedded SMF, however the data became stable in the central region. In this region, the strains measured by OBR are constant and representative of the residual strain in the MEX fabricated specimen. In measurement of G14, the length of stable strain section was again longer than that of G12, meanwhile the scattered outliers remain in the ingress and egress parts of the SMF. Again, with increasing the specimen length, a similar trend was observed in G15. In conclusion, when the specimen length is too small, the measurement data are mostly noise, making it challenging to pick out true values from the outliers. After increasing the specimen length, noise still exists in the ingress and egress parts of the embedded SMF, but the data in the central region becomes constant and representative. The residual strain values of the central section of embedded SMF do not change with further increasing the specimen length.

A specific filter program can be developed to remove the outliers. The outliers always exist and have highly inconsistent values. The SMF here experiences a large strain gradient (from 0 $\mu\epsilon$ to ca. -5000 $\mu\epsilon$) from the free part (outside the specimen) to the embedded part (inside the specimen) in the edges of specimens. The appearance of outliers or noises in strain gradient region of optical fibers during the OBR test have also been reported by previous researchers [15]. Considering practical applications, ignoring the data of the erratic end sections is suggested as a simple alternative to developing a specific filter program. In this way, the average strain of the central stable section is used as the representative residual strain in MEX. For each specimen size, 4

specimens were tested to verify the repeatability of test data. As seen from Fig. 9 (a) and (b), the residual strains of specimens with different widths and lengths are all approximately -4450 $\mu\epsilon$. The specimen length and width have little effect on the residual strains, besides the erratic end regions. The data from ingress and egress parts of the embedded SMF includes a number of outliers. A certain length of embedded SMF is required to distinguish true values from the outliers at the ends. Experience shows that when the specimen length exceeds 25 mm and the width exceeds 5 mm, the in-situ OBR technology can measure residual strains of specimens generated during the MEX process without much difficulty.

3.3. A simplified description for residual strain creation

Based on the specimen temperature history during MEX and corresponding molecular behavior, a simplified description is presented that captures the key mechanisms of residual strain creation.

3.3.1. Temperature profile and corresponding thermal transitions

The temperature evolution of PLA material during MEX and SMF embedding process was investigated using real-time thermography taken by a FLIR IR camera. In the thermograph of Fig. 10 (a), four white lines, i.e. regions of interest (ROI), were placed from the nozzle tip to the current depositing layer and the adjacent previous deposited layers, respectively. The temperature versus distance of ROI 1 shows the temperature evolution of PLA from leaving the nozzle horizontally, along the length of current layer deposition. The temperatures in ROI 2, 3 and 4 show the temperature evolution of the PLA in the thickness direction, toward the previously deposited layers during MEX. Fig. 10 (c) and (e) shows the DSC heating-cooling thermograms of PLA. No obvious differences can be seen between the DSC curves of original filament and extruded i.e. once solidified PLA. The peaks in DSC curves are related to the glass transition, first cold crystallization, interaction between recrystallization and melting of PLA, respectively. As shown in Fig. 10 (b), the temperature in ROI 1 shows a rapid decline from 160 °C to 56 °C, then decreases slowly to a constant temperature of ca. 30 °C (substrate temperature), with the increasing distance to the nozzle. The original far field PLA filament first melts in the heating chamber, changes from the solid state into the viscous flow and then is extruded off the nozzle. Molten PLA is required to ensure layer to layer adhesion and sufficient wetting of the strain sensor during embedment. The temperature finally drops to constant substrate temperature (below glass transition) during the solidification of PLA, before the hot nozzle approaches this area again during the next MEX process cycle. This thermal cycling experienced by the PLA filament during the MEX process is called melting and rapid cooling cycling [22]. When a new layer is built on this layer, the temperature distributions on ROIs 2, 3 and 4 in Fig. 10 (d) showed a very similar trend. The results show that the already solidified plastic, i.e. extruded PLA, will be partially melted again and cooled down to a constant temperature with the increase of distance to the nozzle. Only the adjoining material of substrate layers less than 0.4 mm to the nozzle, two times of layer thickness, experience partial remelting and cooling cycles. In conclusion, the PLA material first experiences a melting and rapid cooling cycling after being squeezed out from the nozzle, and then encounters repeated remelting and cooling cycles in the heat affect zone within ca. 0.4 mm thickness (ca. two deposited layers deep) during the following process.

3.3.2. Description for the residual strain creation

Based on the discussion above, a simplified description for the residual strain creation reflected by embedded SMF is shown in Fig. 11. In the MEX process, the embedded SMF and surrounding PLA material experience two kinds of thermal cycles:

- i melting and rapid cooling during the printing of the current layer.
- ii remelting and cooling during the printing of subsequent layers.

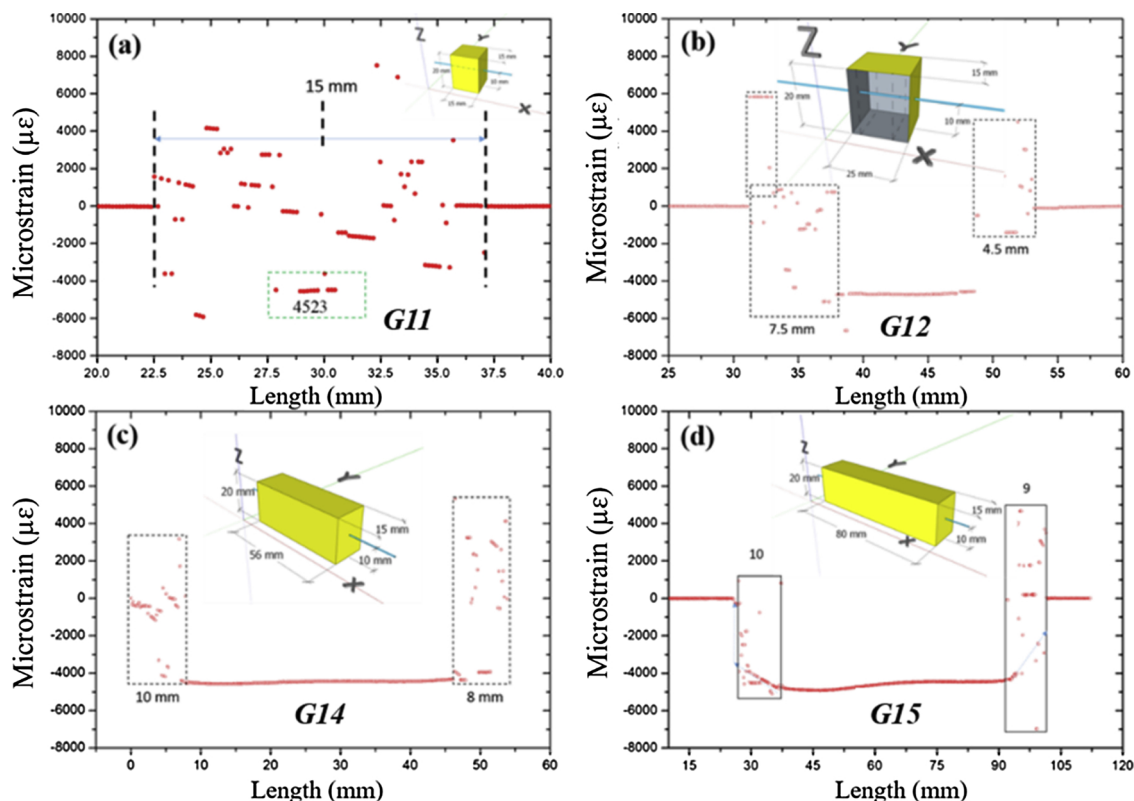


Fig. 8. In-situ OBR measurements of residual strains in MEX specimens with different lengths: (a) 15 mm, (b) 25 mm, (c) 56 mm, (d) 80 mm.

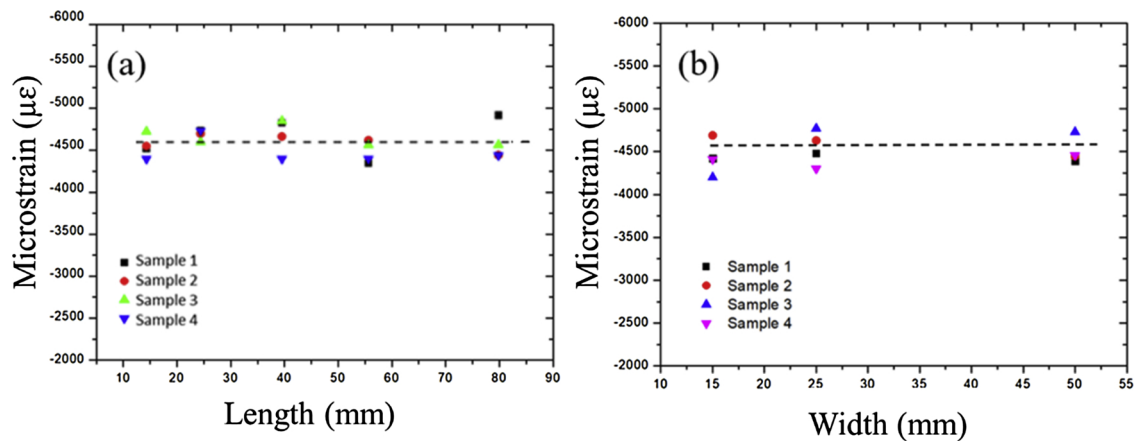


Fig. 9. Average residual strains of MEX fabricated specimens with different lengths (a) and widths (b), data from the central region.

In step 1, before embedding SMF, the PLA is first melted in the heating chamber and extruded out from the nozzle to form the substrate layer. The state of the PLA changes from a semi-molten state to solid during the first melting and rapid cooling. The SMF is placed on the solidified substrate layer before the deposition of a new layer on it. At this moment, the SMF is free from any external strain loading. During step 2, a new layer is built on the solidified substrate PLA layer, where the SMF is laid on. The substrate material in the heat affected zone will remelt. A neck is formed on the interface between the substrate and the new layer, wetting the SMF at the same time. On a molecular level, molecules diffuse, forming an interfacial zone that encapsulates the SMF, and/or forms chemical bonding across the PLA/PLA interface [22]. The bonding between the PLA and polyimide coating is of secondary/physical (i.e. non-covalent) type. The new layer, the substrate layers below, and the SMF in the middle are welded together during the cooling of the interface layer. Residual strain is generated due to the

phase transformation of deposited layers. In step 3 and subsequent steps, the next new layers will be built on the layer encapsulating the SMF. The sensing region will be shortly influenced by the remelting and cooling cycles until it is outside of the heat affected zone. Before removing from the hotbed, the specimen is continuously heated by the hot bed/nozzle and cooled by ambient cold air, resulting in non-uniform thermal gradients inside the 3-D printed structure. Finally, the whole specimen integrated with SMF is detached from the hotbed and cools down to room temperature. The contraction of embedded SMF is only induced by the filament material volumetric shrinkage due to its cooling during MEX. The fabrication induced residual strain is a compressive strain mainly determined by phase transformation and thermal cycles during the MEX process. In a 100 % infilled specimen, each section of SMF is encapsulated by the same amount of PLA roads with the same mesostructure (i.e. contacting surface area and air gap) within the same layer. Because of the characteristic manufacturing of MEX, the

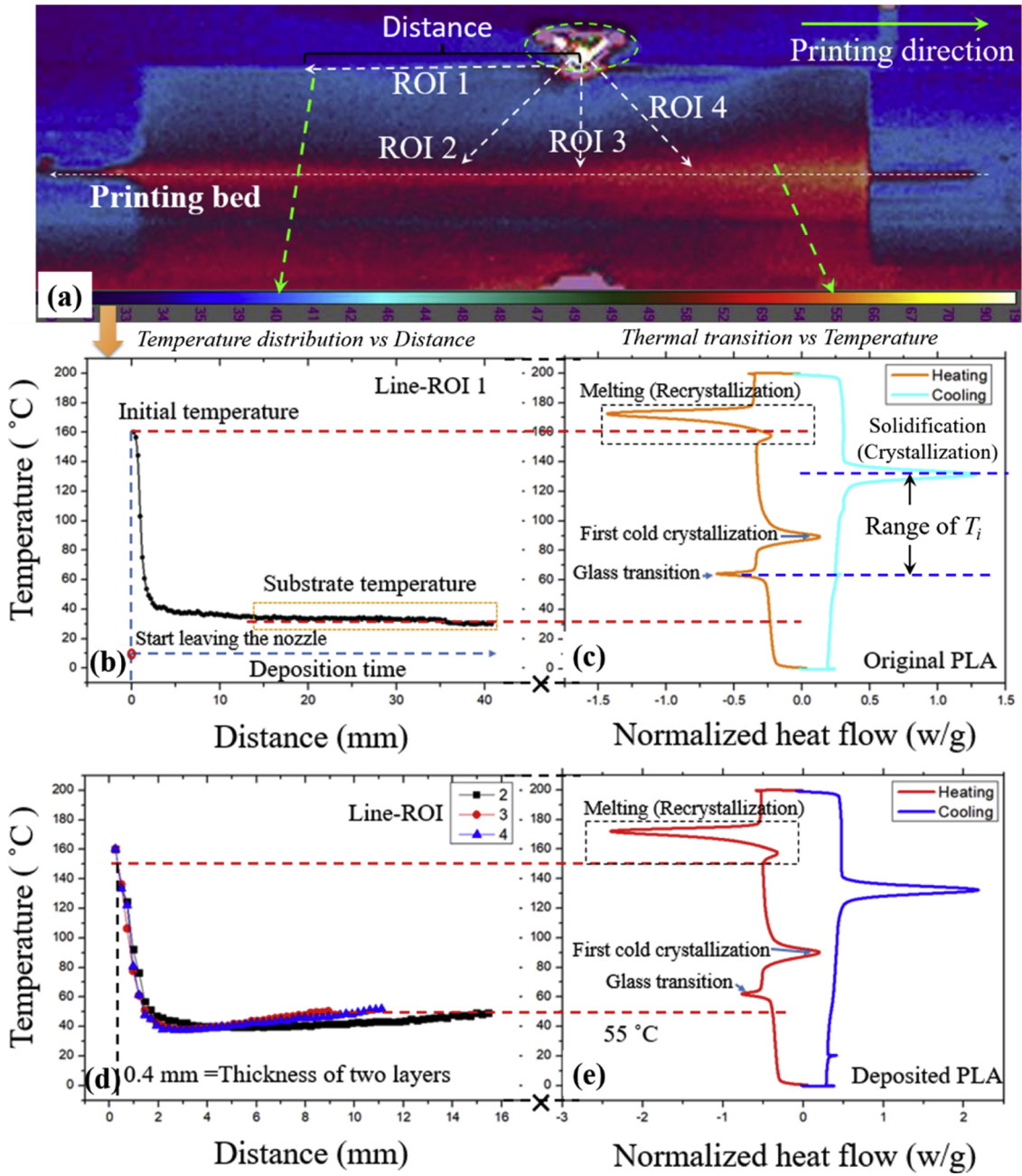


Fig. 10. Thermograph of the specimen during the MEX process (a), temperature distributions and corresponding DSC thermal transitions of original PLA (b)-(c) and deposited PLA (d)-(e).

PLA roads in the same layer experience almost the same phase transformation and thermal cycles individually, resulting in a horizontally uniform distribution of residual strains.

3.3.3. Numerical validation

The OBR measurement results should ideally be validated by comparing the results with the state of the art, but no similar experiments have been reported. Thus, a numerical validation by Monte Carlo sampling of the experimental test results in this research was adopted. As discussed above, the residual strains measured by SMF are mainly induced by the PLA volumetric shrinkage during the MEX process. A theoretically reasonable value range of the residual strain can be approximated by the coefficient of thermal expansion (CTE) of the material. The PLA surrounding the SMF is assumed as an isotropic material, then the volumetric CTE is three times the linear CTE in one

direction since the SMF is believed to be inert to the radial strain. Thus, the residual strain measured ϵ_{OBR} by SMF can be estimated by the following formula:

$$\epsilon_{OBR} = \frac{\Delta V}{3V} = \frac{\Delta L}{L} = \int_{T_i}^{T_f} \alpha_L(T) dT \quad (8)$$

Where α_L is the linear CTE, T_i and T_f are the initial and final temperatures respectively.

The T_f , i.e. room temperature, is already known as 20 °C, while the initial temperature T_i depends on when the effective connection between the SMF and PLA is established. The accurate value of T_i is highly process specific and unknown. According to Fig. 10 (b)-(c), the T_i should exist between solidification and glass transition temperatures, i.e. 130 °C to 60 °C. The α_L value can be estimated between 30×10^{-6} to 85×10^{-6} m/m·K from 3D printing material suppliers in the market. Fig.12 (a) shows 100,000 possible residual strain values calculated

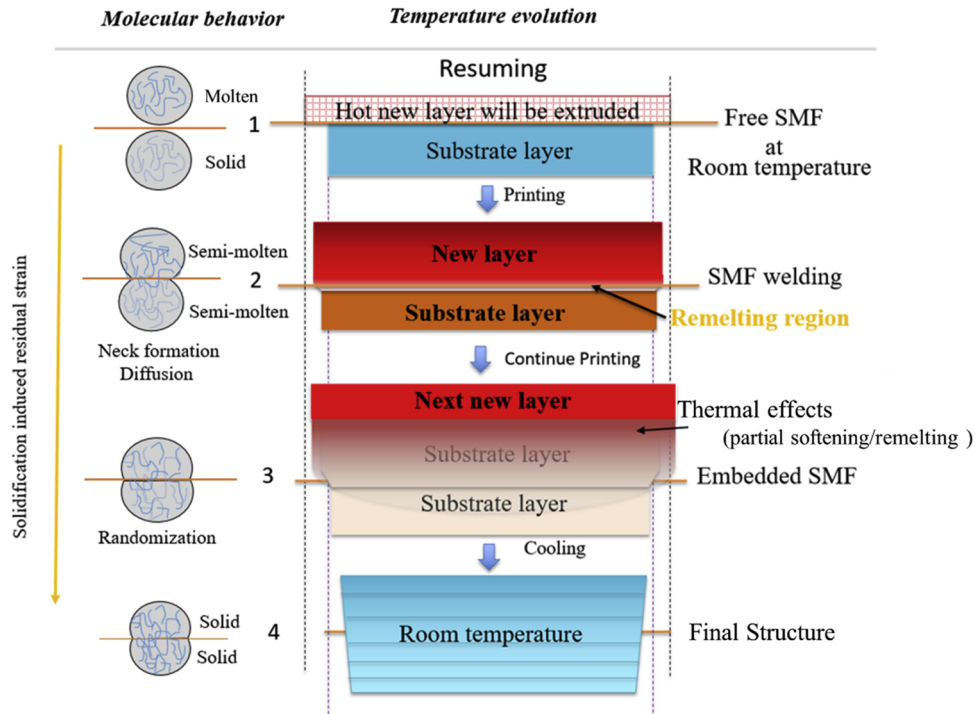


Fig. 11. Simplified description of residual strains creation in MEX and its measurement by in-situ OBR technology.

using Eq. (8) by Monte Carlo sampling. The values of T_i and α_l were selected uniformly from their regions as shown in Fig.12 (b) and (c). The OBR measurement residual strain values (from Fig. 9) were included in the region of numerically calculated values. Fig. 12 (d) shows the distribution statistics of the numerically calculated residual strains, while the OBR measurement values are close to the bar of maximum

number of results.

3.4. Manufacturing defect detection

One of the advantages of in-situ OBR measurements is the ability of detecting internal defects during the MEX process. By internal

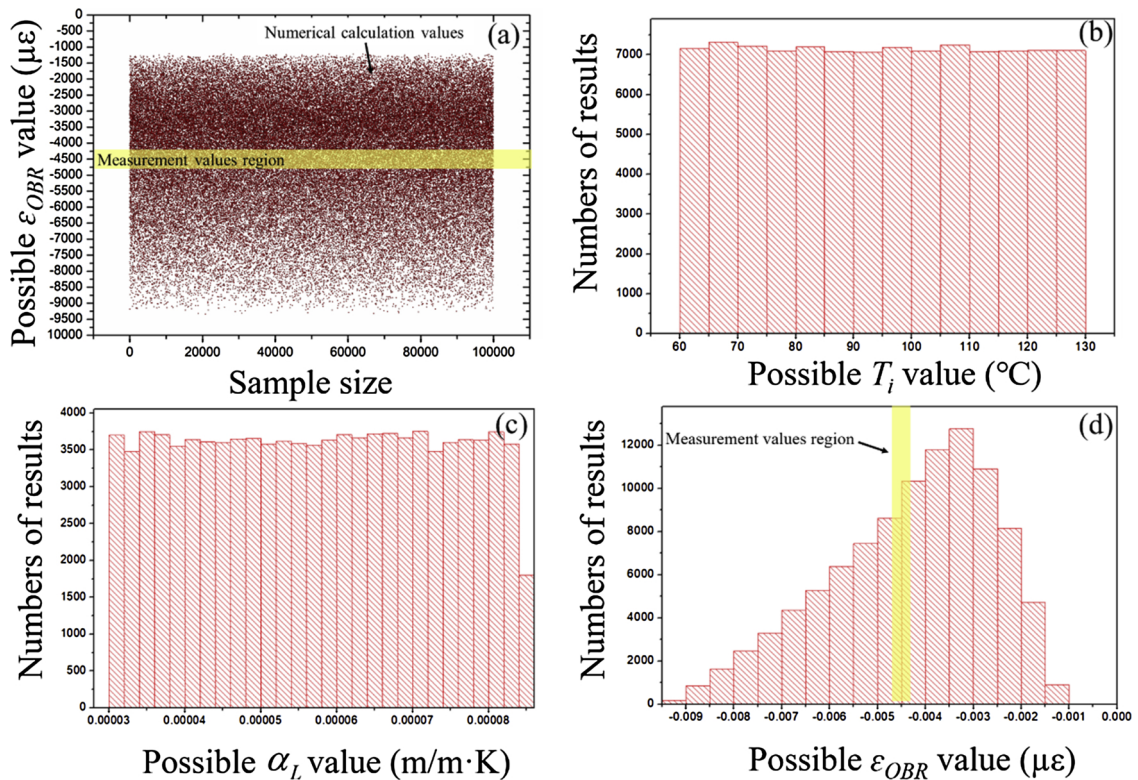


Fig. 12. Numerical predictions vs. OBR measurement results of residual strains: (a) Numerically calculated values, (b) Distribution statistics of T_i , (c) Distribution statistics of α_l , (d) Distribution statistics of the Monte Carlo sampling results.

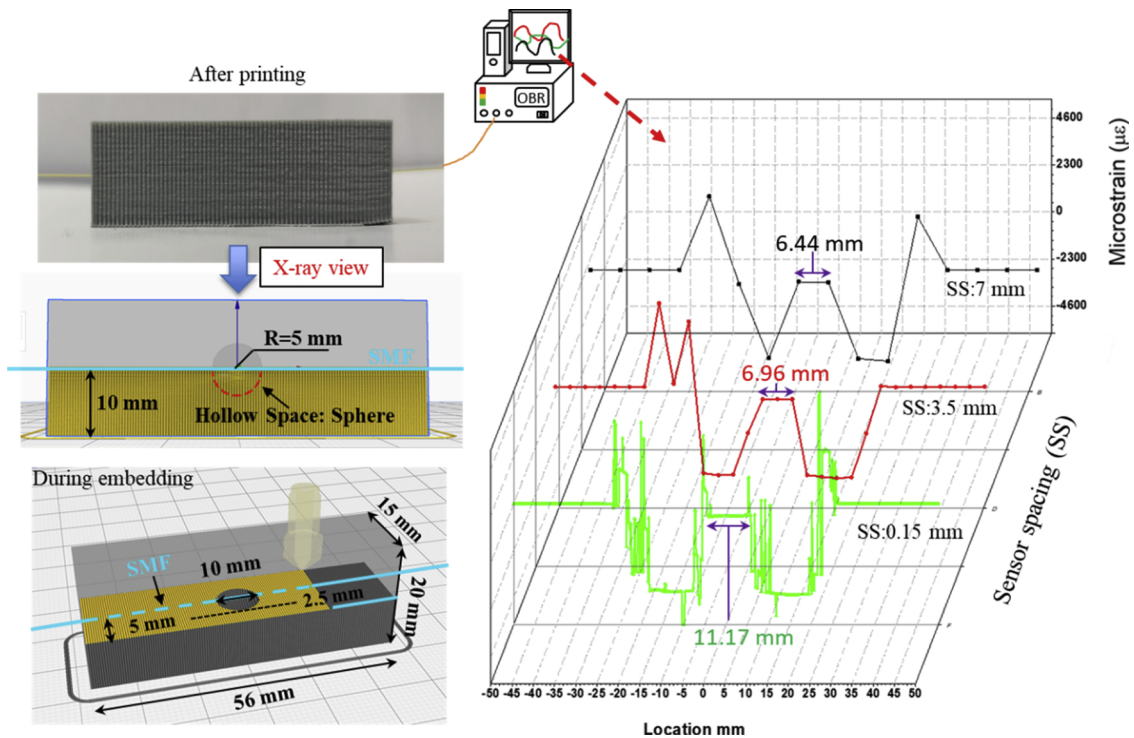


Fig. 13. A schematic illustration of a predesigned defect inside the specimen and corresponding measurement results from the OBR.

manufacturing defects we hereby mean voids in 100 % infill specimens. The reference residual strain distribution in a MEX fabricated specimen (without defects) can be obtained from previous results. By comparing it with the measurement results of specimens with a void defect, the location and the size of the void can be identified non-destructively with in-situ OBR technology.

In this study, one specimen was predesigned with a hollow sphere void ($\varnothing = 10$ mm) in the specimen center to mimic a manufacturing defect. A SMF fiber was embedded in the midplane of the printed block as shown in Fig. 13(left). After printing, the residual strains in the specimen were processed with $GL = 7$ mm and SS values at 7 mm, 3.5 mm and 0.15 mm, respectively. The result is shown in Fig.13 (right). Different to the usual residual strain distribution, a sudden reduction in strains appears in the center of the specimen. The strain curve drops close to zero and then keeps flat for 6 mm–10 mm before restoration. The length and position of the distorted section coincides with the predesigned defect. With the decrease of SS , the location of the defect didn't change, but the length became more exact, showing higher spatial resolution. Notably, the measurement noise appears nearby the two sides of defect regions. This is consistent with previous test results regarding the ingress and egress parts of the embedded SMF. Thus the experiment here demonstrates the possibility of identifying manufacturing defects by this new OBR approach. Measuring fine scale abrupt local changes in strains with OBR can become difficult due to noise problems.

4. Conclusions

In this work, a novel approach for in-situ measurements of the solidification induced residual strain distribution in MEX fabricated specimens was demonstrated for the first time. Optical backscatter reflectometry (OBR) based fiber-optic sensing system was embedded to measure distributed residual strains. The practical challenges, validity and reliability of the developed approach were investigated. The experimental OBR measurement results are summarized as follows:

1 The microscopy observations and DSC testing showed that the SMF

is well encapsulated by the PLA and the presented embedding procedure is non-invasive in both micro- and macro-scale. The tensile test showed that the SMF/matrix interface is uniform and enables the SMF to work as a reliable distributed strain sensor at least up to 10,000 $\mu\epsilon$. The in-situ OBR strain data shows fair agreement with point measurement from electrical strain gauges.

- 2 The horizontal inplane size (length and width) of the sample brings minor effects on the measurement results. A noise region is always present in the egress and ingress part of the embedded SMF, whereas the signals from the center region are constant and representative. The OBR can be adopted as a reliable in-situ measurement method for residual strains, when the embedding length of SMF is longer than 25 mm.
- 3 The temperature evolution, measured by the IR camera, showed that the PLA material experiences several melting and rapid cooling cycles after leaving the nozzle. The residual strains in MEX are mainly created by the contraction of thermoplastics during phase transformation induced by thermal cycles. Because of the special manufacturing method of MEX, the residual strain value in each point of the same layer is almost the same, resulting in a horizontally uniform distribution of residual strains. In the vertical direction (height), the average residual strain values show a parabolic trend. Largest residual strain occurs inside the bulk of the specimen at ca. 1/3 height from the heat bed.
- 4 A hollow sphere located in the center of the 100 % infill specimen was predesigned to mimic a manufacturing defect i.e. a large void. The in-situ OBR technology was able to detect this manufacturing defect successfully. The method shows a good potential for future applications in production property assessment from 3D printing.

Funding

This research did not receive any specific grant from funding agencies in the public, commercial, or not-for-profit sectors.

CRedit authorship contribution statement

Shaoquan Wang: Conceptualization, Data curation, Formal analysis, Investigation, Methodology, Software, Validation, Visualization, Writing - original draft, Writing - review & editing. **Kaspar Lasn:** Project administration, Resources, Supervision, Funding acquisition, Writing - original draft, Formal analysis. **Christer Westum Elverum:** Writing - original draft, Writing - review & editing, Supervision. **Di**

Wan: Writing - review & editing, Investigation. **Andreas Echtermeyer:** Writing - original draft, Writing - review & editing, Resources, Supervision.

Declaration of Competing Interest

None.

Appendix A. Post-processing parameters effects on strain measurements

In OBR, two parameters, i.e. gauge length (GL) and sensor spacing (SS) need to be defined for the post processing program. To analyze the influence of post-processing parameters, the same measurement data was processed with different GL and SS values. When SS was set to a constant 5 mm, the strain values with different GL from 4 mm to 50 mm show a similar pattern and an average value at about $-4444 \mu\epsilon$ as seen in Table A1. But the sensing length, which was the distance between the start point and end point of the bathtub, decreases slightly with increasing GL (see in Fig. A1 (a)). When the GL is set to 4 mm, the sensing length is closest to the real length of the specimen. The spatial resolution of the strain measurement is mainly influenced by SS. A constant GL of 4 mm interacting with five SS values were also tested: 4 mm, 2 mm, 1 mm, 0.5 mm, and 0.15 mm, thus representing 14, 28, 56, 112 and 374 measuring points, respectively. As shown in Fig. A1 (b), using a smaller SS, a strain map with higher spatial resolution is achieved, however more noise peaks also emerge in the results. The strain values from different SS sets are analyzed statistically and presented in Table A2. All mean strains were ca. $1000 \mu\epsilon$ smaller than the average strains in Table A1. It is notable that calculated standard deviations of each set were very large compared with the mean strain. The obvious distortion of the measured data is due to the relatively erratic measurements in the ingress and egress part of the embedded SMF, i.e. the ends of the bathtub. After removing the data from the ingress and egress part from the consideration, the mean strain became again very close to $-4444 \mu\epsilon$, while the standard deviations of the reintegrated data of different sets are very small as shown in second half of Table A2. Therefore, it is concluded that a very high spatial resolution at mm level can be accomplished by selecting appropriate GL and SS. The disadvantage of a high spatial resolution mode is the presence of the noise. Noisy data should be identified - here at the ingress/egress locations - and removed from further consideration. Based on the obtained results, the minimum SS, i.e. spatial resolution, and GL for the in-situ OBR system adopted in this research are 0.15 mm and 4 mm, respectively.

Table A1

Residual strain values from different GL (SS = 5 mm = Const.), at the bathtub bottom.

GL (mm)	4	16	30	50
Average strain ($\mu\epsilon$)	-4429	-4458	-4457	-4432
Standard deviations ($\mu\epsilon$)	93	59	56	8
Sensing length (mm)	60	55	44	34

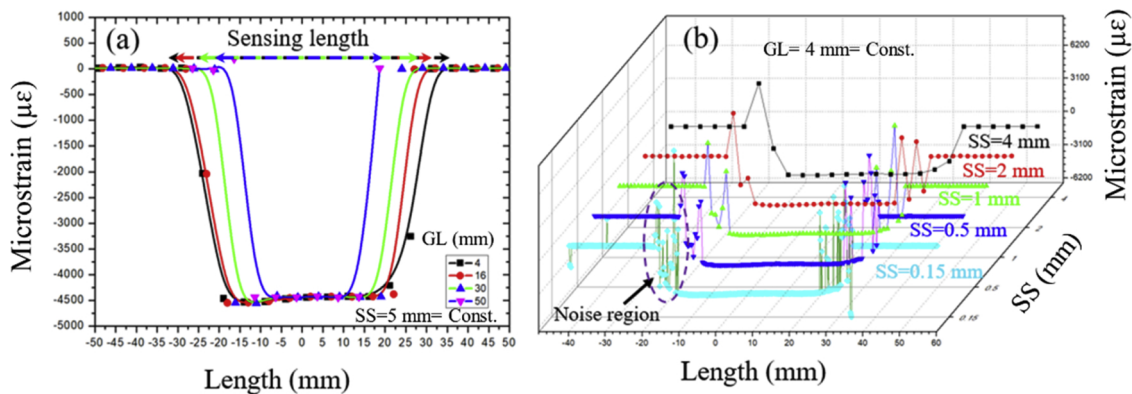


Fig. A1. Residual strain distribution in MEX fabricated specimens: (a) Influence of GL parameter on the results, (b) Influence of SS parameter on the results.

Table A2

Residual strain values from different SS (GL = 4 mm = Const.), at the bathtub bottom.

Statistical property	SS (mm)	4	2	1	0.5	0.15
Original	Average strain ($\mu\epsilon$)	-3561	-3487	-3601	-3546	-3623
	Standard deviations ($\mu\epsilon$)	2294	2233	2225	2286	2110
Disregarding noise regions	SS (mm)	4	2	1	0.5	0.15
	Average strain ($\mu\epsilon$)	-4473	-4477	-4479	-4481	-4483
	Standard deviations ($\mu\epsilon$)	53	56	56	54	55

References

- [1] H. Bikas, Panagiotis Stavropoulos, George Chryssolouris, Additive manufacturing methods and modelling approaches: a critical review, *Int. J. Adv. Manuf. Technol.* 83 (1-4) (2016) 389–405.
- [2] Pedram Parandoush, Dong Lin, A review on additive manufacturing of polymer-fiber composites, *Compos. Struct.* 182 (2017) 36–53.
- [3] Hongbin Li, Taiyong Wang, Qing Li, Zhiqiang Yu, Wang Na, A quantitative investigation of distortion of polylactic acid (PLA) part in MEX from the point of inter-fiber residual stress, *Int. J. Adv. Manuf. Technol.* 94 (1-4) (2018) 381–395.
- [4] C. Kousiatza, D. Karalekas, In-situ monitoring of strain and temperature distributions during fused deposition modeling process, *Mater. Des.* 97 (2016) 400–406, <https://doi.org/10.1016/j.matdes.2016.02.099>.
- [5] Q. Dao, J.C. Frimodig, Li X.-Z. Le HN, S.B. Putnam, K. Golda, et al., Calculation of shrinkage compensation factors for rapid prototyping (MEX 1650), *Comput. Appl. Eng. Educ.* 7 (1999) 186–195, [https://doi.org/10.1002/\(SICI\)1099-0542\(1999\)7:3<186::AID-CAE7>3.0.CO;2-Q](https://doi.org/10.1002/(SICI)1099-0542(1999)7:3<186::AID-CAE7>3.0.CO;2-Q).
- [6] Caterina Casavola, Alberto Cazzato, Vincenzo Moramarco, Giovanni Pappalettera, Residual stress measurement in Fused Deposition Modelling parts, *Polym. Test.* 58 (2017) 249–255.
- [7] Y. Zhang, K. Chou, A parametric study of part distortions in fused deposition modelling using three-dimensional finite element analysis, *Proc. Inst. Mech. Eng. Part B J. Eng. Manuf.* 222 (2008) 959–968, <https://doi.org/10.1243/09544054JEM990>.
- [8] O.S. Es-Said, J. Foyos, R. Noorani, Mel Mendelson, R. Marloth, B.A. Pregger, Effect of layer orientation on mechanical properties of rapid prototyped samples, *Mater. Manuf. Process.* 15 (1) (2000) 107–122.
- [9] Tian-Ming Wang, Jun-Tong Xi, Jin Ye, A model research for prototype warp deformation in the MEX process, *Int. J. Adv. Manuf. Technol.* 33 (11-12) (2007) 1087–1096.
- [10] A. Kantaros, D. Karalekas, Fiber Bragg grating based investigation of residual strains in ABS parts fabricated by fused deposition modeling process, *Mater. Des.* 50 (2013) 44–50, <https://doi.org/10.1016/j.matdes.2013.02.067>.
- [11] C. Kousiatza, D. Tzetzis, D. Karalekas, In-situ characterization of 3D printed continuous fiber reinforced composites: a methodological study using fiber Bragg grating sensors, *Compos. Sci. Technol.* 174 (2019) 134–141, <https://doi.org/10.1016/j.compscitech.2019.02.008>.
- [12] M. Froggatt, J. Moore, High-spatial-resolution distributed strain measurement in optical fiber with Rayleigh scatter, *Appl. Opt.* 37 (1998) 1735–1740, <https://doi.org/10.1364/AO.37.001735>.
- [13] C.K.Y. Leung, K.T. Wan, D. Inaudi, X. Bao, W. Habel, Z. Zhou, J. Ou, M. Ghandehari, H.C. Wu, M. Imai, Review: Optical fiber sensors for civil engineering applications, *Mater. Struct.* 48 (2013) 871–906, <https://doi.org/10.1617/s11527-013-0201-7>.
- [14] J.-M. Henault, G. Moreau, S. Blairon, J. Salin, J.-R. Courivaud, F. Taillade, E. Merliot, J.-P. Dubois, J. Bertrand, S. Buschaert, et al., Truly distributed optical fiber sensors for structural health monitoring: from the telecommunication optical fiber feedstocking tower to water leakage detection in dikes and concrete structure strain monitoring, *Adv. Civ. Eng. Mater.* 2010 (2010), <https://doi.org/10.1155/2010/930796>.
- [15] Søren Heinze, Andreas Echtermeyer, In-situ strain measurements in large volumes of hardening epoxy using Optical Backscatter Reflectometry, *Appl. Sci.* 8 (7) (2018) 1141.
- [16] Astrid Billon, Jean-Marie Henault, Marc Quiertant, Frédéric Taillade, Aghiad Khadour, Renaud-Pierre Martin, Karim Benzarti, Quantitative strain measurement with distributed fiber optic systems: qualification of a sensing cable bonded to the surface of a concrete structure, In EWSHM-7th European Workshop on Structural Health Monitoring (2014).
- [17] V. Villalba, J.R. Casas, S. Villalba, Application of OBR fiber optic technology in structural health monitoring of Can Fatjó Viaduct (Cerdanyola de Vallés-Spain), Proceedings of the VI International Conference on Bridge Maintenance, Safety and Management, Lake Maggiore, Italy. 8–12 July, 2012.
- [18] Jon Grave, L. Harald, Magnus L. Håheim, Andreas T. Echtermeyer, Measuring changing strain fields in composites with distributed Fiber-Optic sensing using the optical backscatter reflectometer, *Compos. Part B Eng.* 74 (2015) 138–146.
- [19] Stephen T. Kreger, Dawn K. Gifford, Mark E. Froggatt, Brian J. Soller, Matthew S. Wolfe, High resolution distributed strain or temperature measurements in single- and multi-mode fiber using swept-wavelength interferometry, *Optical Fiber Sensors*, p. ThE42, Optical Society of America, 2006.
- [20] Erik Saeter, Kaspar Lasn, Fabien Nony, Andreas T. Echtermeyer, Embedded optical fibres for monitoring pressurization and impact of filament wound cylinders, *Compos. Struct.* 210 (2019) 608–617.
- [21] Taylan Örs, Fanny Gouraud, René Guinebretière, Marc Huger, Vincent Michel, Olivier Castelnau, Neutron diffraction measurements of residual stress distribution in large zirconia based refractory bricks produced by electro-fusion and casting, *J. Eur. Ceram. Soc.* 37 (5) (2017) 2295–2302.
- [22] Lourens G. Blok, Marco L. Longana, H. Yu, Ben K.S. Woods, An investigation into 3D printing of fibre reinforced thermoplastic composites, *Addit. Manuf.* 22 (2018) 176–186.
- [23] Sigmund A. Tronvoll, Nils Petter Vedvik, Christer W. Elverum, Torgeir Welo, A new method for assessing anisotropy in fused deposition modeled parts using computed tomography data, *Int. J. Adv. Manuf. Technol.* 105 (1-4) (2019) 47–65.